

# Ultra-low frequency gravitational waves: distinguishing cosmological backgrounds from astrophysical foregrounds

Christopher J. Moore<sup>1</sup> Alberto Vecchio,<sup>1</sup>

<sup>1</sup>*Institute for Gravitational Wave Astronomy & School of Physics and Astronomy, University of Birmingham, Edgbaston, Birmingham B15 2TT, UK*

14 March 2022

## ABSTRACT

The gravitational wave (GW) spectrum at frequencies below  $\sim 100$  nHz may contain overlapping contributions from processes in the early Universe and black hole binaries with masses  $\sim 10^6 - 10^9 M_\odot$  at low redshifts. Pulsar timing arrays are measuring the GW background at  $\sim 1 - 100$  nHz, but are currently unable to distinguish an astrophysical foreground from a cosmological background due to, say, a first order phase transition at a temperature  $\sim 1 - 100$  MeV in a weakly-interacting dark sector. Our analysis reveals the extent to which including integrated bounds on the ultra-low frequency GW spectrum from cosmic microwave background, big bang nucleosynthesis or astrometric observations can break this degeneracy.

Gravitational waves (GWs) at ultra-low frequencies (below 100 nHz) are key to understanding the assembly and evolution of massive black holes (BHs). These GWs also offer a window into a variety of early Universe processes that may be inaccessible by other means as they occur before decoupling at which point the Universe becomes transparent. The ability to distinguish between these overlapping contributions is vital to interpreting the signal that may be observed.

Ultra-low frequency GWs are difficult to observe directly due partly to the necessity of observations spanning several years, or decades. The primary technique, proposed in the 1970s (Sazhin 1978; Detweiler 1979; Foster & Backer 1990), uses millisecond pulsars as a network of extremely stable clocks, the arrival time of whose “ticks” are ever so slightly perturbed by GWs.

A stochastic GW signal – either of astrophysical (foreground) or cosmological (background) origin – can be described in terms of the dimensionless energy density per logarithmic unit of frequency,

$$\hat{\Omega}_{\text{GW}}(f) = \frac{1}{\rho_c} \frac{d\rho(f)}{d \ln f} = \frac{2\pi^2}{3H_0^2} f^2 h_c^2(f). \quad (1)$$

Here,  $\rho_c$  is the critical density of the Universe,  $\rho(f)$  is the energy density in GWs at frequency  $f$ , and  $H_0 = 67.4 \text{ km s}^{-1} \text{ Mpc}^{-1}$  is the Hubble constant (Planck Collaboration 2020). As shown above,  $\hat{\Omega}_{\text{GW}}(f)$  is related to the characteristic strain,  $h_c(f)$ , commonly used in the GW literature.

Pulsar timing arrays (PTAs) directly measure  $\hat{\Omega}_{\text{GW}}(f)$  in the frequency range  $1 - 100$  nHz. Several collaborations have now undertaken a twenty year campaign of radio observations of  $\sim 100$  of the most stable millisecond pulsars, resulting in a steadily improving sensitivity to GWs (Shannon et al. 2015; Lentati et al. 2015; Verbiest et al. 2016; Arzoumanian et al. 2018). The NANOGrav collaboration recently reported evidence for a common stochastic process among the 45 millisecond pulsars in their 12.5 year data set consistent with an astrophysical GW background with  $\hat{\Omega}_{\text{GW}}(f_{\text{yr}}) = 2.6 - 9.8 \times 10^{-9}$  (blue line in Fig. 1) where  $f_{\text{yr}} = \text{year}^{-1}$  (Arzoumanian et al. 2020). PTA measurements are discussed further in appendix A. Although this is not yet a clear detection, we assume that it is indeed a GW signal. The signal is consistent both with an astrophysical foreground from massive ( $\sim 10^6 - 10^9 M_\odot$ ) BH binaries (Middleton et al. 2021)

and a cosmological background generated by, for example, primordial BHs, cosmic strings, or dark-sector phase transitions (see, for example, De Luca et al. 2021; Vaskonen & Veermäe 2021; Ellis & Lewicki 2021; Blasi et al. 2021; Nakai et al. 2021; Ratzinger & Schwaller 2021; Addazi et al. 2020; Schwaller 2015).

Other observations indirectly constrain the *integrated* GW spectrum; i.e. the total energy across a wide range of frequencies,

$$\Omega_{\text{GW}} = \int_{f_{\text{min}}}^{f_{\text{max}}} \frac{df}{f} \hat{\Omega}_{\text{GW}}(f). \quad (2)$$

Several indirect probes independently place constraints at the level  $\Omega_{\text{GW}} \lesssim 10^{-6}$  over different ultra-low frequency ranges (dashed black arrows in Fig. 1). The energy in a GW background effects the growth of density perturbations as well as the cosmological expansion rate at the time of decoupling. Therefore, CMB observations from WMAP or Planck, in combination with other large-scale structure surveys, are able to place integrated constraints on  $\Omega_{\text{GW}}$  (Clarke et al. 2020; Smith et al. 2006) with  $f_{\text{min}} \sim 10 - 100 f_{\text{Hubble}}$ , where  $f_{\text{Hubble}} = H_0$ . Elsewhere, the success of big bang nucleosynthesis (BBN) predictions for the primordial abundances of light elements constrains extra, unbudgeted energy (including GWs) at the time of nucleosynthesis. As BBN occurs before recombination, at a temperature  $T_{\text{BBN}} \sim 1$  MeV, this only constrains the GW spectrum above  $f_{\text{min}} = f_{\text{BBN}} \sim 10^{-10} \text{ Hz}$  (Cooke et al. 2014; Maggiore 2018). Both the CMB and BBN bounds probe GWs in the early Universe and are insensitive to those produced later by astrophysical processes. Furthermore, both bounds depend on assumptions such as the density distribution of perturbations and the effective number of neutrino species, and probe the GW background only indirectly; these early Universe constraints are reviewed in appendix B1.

Astrometry is the only other technique directly sensitive to ultra-low frequency GWs at a level potentially competitive with the aforementioned probes. Photons from extragalactic sources, following null geodesics in the background metric, are deflected by ultra-low GWs causing changes in the apparent positions (i.e. proper motions) of distant objects. Very long baseline interferometry (VLBI) observations of the proper motions of a few hundred quasars taken over several years place an upper limit of  $\Omega_{\text{GW}} \lesssim 6 \times 10^{-3}$  (Darling

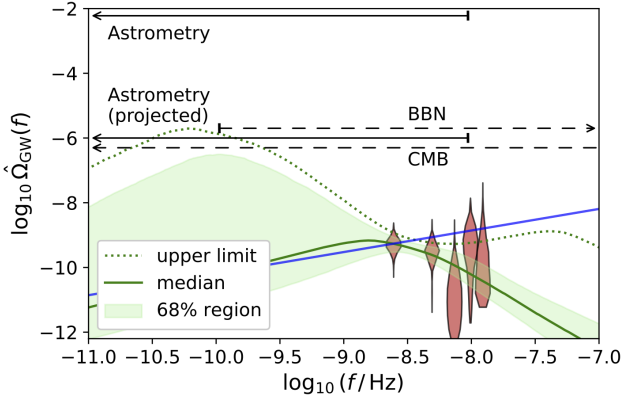


**Figure 1.** Red histograms show NANOGrav posteriors on the energy density  $\hat{\Omega}_{\text{GW}}(f)$  in the 5 lowest frequency bins. Horizontal arrows show the integrated bounds on the total energy  $\Omega_{\text{GW}}$  discussed in the text; integrated bounds span the frequency ranges indicated by the arrows and are not directly comparable with the density. Dashing distinguishes indirect bounds that apply only at high redshifts from local, direct bounds. The blue line shows the median spectrum obtained from the NANOGrav results assuming a BH astrophysical foreground origin for the signal with  $\hat{\Omega}_{\text{GW}} \propto f^{2/3}$ . The green line shows our median reconstructed spectrum based on the PTA-only data, assuming a cosmological PT background. The shaded region (dotted line) indicates the  $\pm 1 \sigma$  uncertainty (95% upper limit) on the PT spectrum. Unlike the astrophysical foreground, the PT background peaks below the reach of PTAs and is further constrained by the integrated bounds. For a similar posteriors on the characteristic strain spectrum,  $h_c(f)$ , see appendix D.

et al. 2018) on GWs below a frequency set by the span of observations,  $f_{\text{max}} \sim (3 \text{ year})^{-1}$ . The projections are that this might be improved to as low as  $\lesssim 10^{-6}$  by the end of the Gaia mission (Book & Flanagan 2011) using a greatly expanded catalog of quasars. The astrometric bounds are plotted using solid arrows in Fig. 1. Astrometric observations directly constrain GWs in the local Universe, which includes any produced by astrophysical processes after recombination, and distinguishes them from other forms of energy [astrometry even distinguishes between different possible GW polarisations; e.g. (Mihaylov et al. 2018)]. Astrometric observations are reviewed in appendix B2.

The astrophysical prediction (e.g. Sesana et al. 2008; Sesana 2013; Kelley et al. 2017) is for a blue spectrum from inspiralling massive BH binaries with  $\hat{\Omega}_{\text{GW}}(f) \propto f^{2/3}$  in the PTA band (blue line in Fig. 1). The signal is expected to be dominated by BH binaries in the mass range  $\sim 10^6 - 10^9 M_{\odot}$  out to redshifts  $z \sim 2$ . However, the NANOGrav data are also consistent with a red spectrum, e.g. from a phase transition (PT).

In this letter, we show the importance of including integrated bounds by using two example model spectra. We consider these two models to be proxies for a wide range of possible exotic physics.

We start by considering the particular PT model of Caprini et al. (2009); Jinno & Takimoto (2017); Hindmarsh et al. (2017) which is here determined to occur in the temperature range  $\approx 1 - 300 \text{ MeV}$ . In order to be consistent with standard model physics at these low collider energies, the transition must occur in a *dark sector*, decoupled from the standard model. GWs are generated during the PT by collisions of bubbles and sound waves, as well as turbulence. The PT spectrum fitted only to the NANOGrav data (green line in Fig. 1) allows for peaks below  $\sim 1 \text{ nHz}$  and (at 85% confidence) for  $\Omega_{\text{GW}} > 10^{-6}$ . As has been pointed out by Arzoumanian et al. (2021), PTA measurements alone are currently unable to distinguish this background from

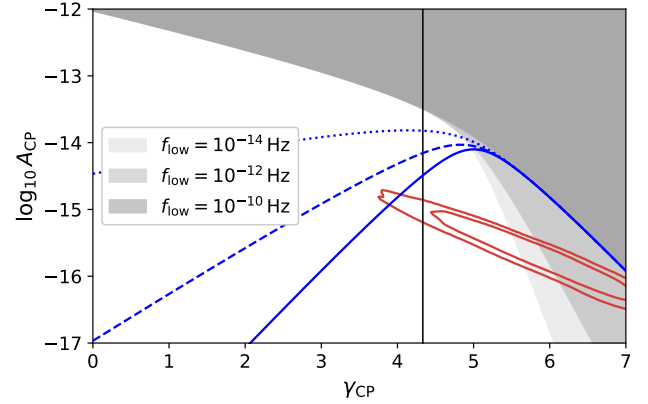


**Figure 2.** Red contours indicate PTA-only posteriors on the power-law spectrum amplitude and slope parameters. The vertical line indicates the astrophysical prediction,  $\gamma_{\text{CP}} = 13/3$ . The NANOGrav posterior is consistent with larger  $\gamma_{\text{CP}}$  (i.e. redder spectra with large  $\hat{\Omega}_{\text{GW}}(f)$  at low frequencies) which are ruled out by an integrated constraint,  $\Omega_{\text{GW}} < 10^{-6}$ , as shown by the shaded regions (this constraint depends on the low frequency cutoff,  $f_{\text{low}}$ , of the spectra). The integrated constraint also helps to rule out bluer spectra (although these are anyway mostly incompatible with the PTA measurements) as shown by the constraints plotted in blue which depend on a high frequency cutoff in the spectra; results are shown for  $f_{\text{high}} = 10^{-5} \text{ Hz}$  (solid),  $f_{\text{high}} = 10^{-6} \text{ Hz}$  (dashed), and  $f_{\text{high}} = 10^{-5} \text{ Hz}$  (dotted).

an astrophysical foreground. However, including integrated bounds from CMB, BBN and astrometry further constrains the PT model. In appendix C we describe our analysis of the NANOGrav data using the PT models described in Arzoumanian et al. (2021), both with and without the inclusion of an integrated bound,  $\Omega_{\text{GW}} < 10^{-6}$ . Although the integrated bound is insufficiently constraining to completely rule out the PT model, we find it does eliminate a significant extra fraction of the PT model parameter space (see Fig. 3).

Additionally, we perform a separate analysis for a simple power-law GW spectrum,

$$h_c(f) = A_{\text{CP}}(f/f_{\text{yr}})^{\alpha_{\text{CP}}}, \quad \text{for } f_{\text{low}} < f < f_{\text{high}}. \quad (3)$$

where  $\alpha_{\text{CP}} = (3 - \gamma_{\text{CP}})/2$ . The NANOGrav results alone are consistent with a range of spectral slopes that allow for a variety of possible early-Universe interpretations. In fact, the data favours a spectrum redder than the astrophysical prediction. We find that the inclusion of an integrated constraint remains consistent with an astrophysical interpretation of the signal but helps to rule out extremely red spectra (see Fig. 2), although the exact constraint is sensitive to the placement of the low frequency cutoff of the spectrum.

In summary, with a detection imminent (Pol et al. 2020), it is necessary to separate clearly the astrophysical foreground from a variety of possible cosmological backgrounds in order to reliably interpret an ultra-low frequency GW signal. This is difficult with PTAs alone due to their limited ability to measure the spectral slope and/or shape [longer term, the IPTA (Perera et al. 2019) and SKA (e.g. Janssen et al. 2015) will increase this ability]. The situation can be improved by consistently combining information from other probes of the ultra-low frequency GW background that place constraints on the integrated spectrum. These include indirect cosmological probes sensitive to GWs (and other relativistic species) at high redshifts as well as astrometric observations that directly constrain GWs produced across all cosmic times. It is therefore important to improve as far as possible these bounds, in particular the direct astrometric bound that can be placed with Gaia in combination with VLBI.

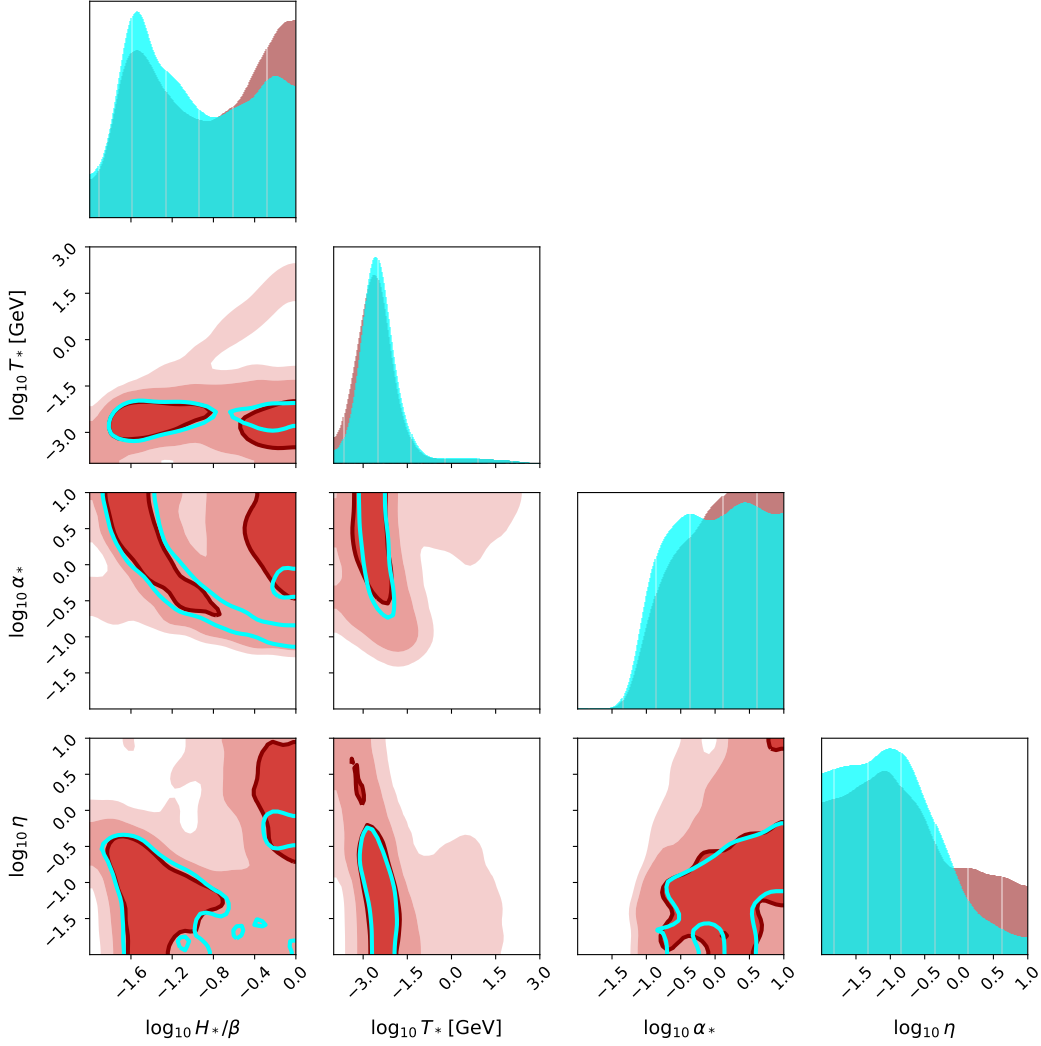


**Figure 3.** Posteriors on the 4 parameters of the PT model: the temperature,  $T_*$ , and strength,  $\alpha_*$ , of the PT, the bubble nucleation rate,  $\beta/H_*$ , in units of the Hubble parameter at the transition, and the dimensionless friction parameter,  $\eta$ . Posteriors obtained from the PTA-only data alone are shown in red. Shown in light blue is the posteriors obtained with the additional integrated constraint  $\Omega_{\text{GW}} < 10^{-6}$ . The integrated constraint further rules out parts of the PT parameter space, in particular regions of large  $\eta$ ,  $\alpha_*$  and  $H_*/\beta$ . This can be seen most clearly by comparing the two 50% contours drawn here with solid red and blue lines. The combined results slightly improve the constraint on the temperature of the transition to be in the range  $T_* \sim 1 - 300$  MeV (10% and 90% quantiles).

## ACKNOWLEDGEMENTS

AV acknowledges the support of the Royal Society and Wolfson Foundation.

## REFERENCES

- Abe K. T., Tada Y., Ueda I., 2020, arXiv e-prints, p. [arXiv:2010.06193](https://arxiv.org/abs/2010.06193)
- Addazi A., Cai Y.-F., Gan Q., Marciano A., Zeng K., 2020, arXiv e-prints, p. [arXiv:2009.10327](https://arxiv.org/abs/2009.10327)
- Arzoumanian Z., et al., 2018, *ApJ*, **859**, 47
- Arzoumanian Z., et al., 2020, *ApJ*, **905**, L34
- Arzoumanian Z., et al., 2021, e-prints, p. [arXiv:2104.13930](https://arxiv.org/abs/2104.13930)
- Blasi S., Brdar V., Schmitz K., 2021, *Phys. Rev. Lett.*, **126**, 041305
- Book L. G., Flanagan É. É., 2011, *Phys. Rev. D*, **83**, 024024
- Braginsky V. B., Kardashev N. S., Polnarev A. G., Novikov I. D., 1990, *Nuovo Cimento B Serie*, **105**, 1141
- Brandenburg A., Clarke E., He Y., Kahniashvili T., 2021, arXiv e-prints, p. [arXiv:2102.12428](https://arxiv.org/abs/2102.12428)
- Caprini C., Durrer R., Servant G., 2009, *J. Cosmology Astropart. Phys.*, **2009**, 024
- Clarke T. J., Copeland E. J., Moss A., 2020, *J. Cosmology Astropart. Phys.*, **2020**, 002
- Cooke R. J., Pettini M., Jorgenson R. A., Murphy M. T., Steidel C. C., 2014, *ApJ*, **781**, 31
- Darling J., Truebenbach A. E., Paine J., 2018, *ApJ*, **861**, 113
- De Luca V., Franciolini G., Riotto A., 2021, *Phys. Rev. Lett.*, **126**, 041303
- Detweiler S., 1979, *ApJ*, **234**, 1100
- Ellis J., Lewicki M., 2021, *Phys. Rev. Lett.*, **126**, 041304
- Foster R. S., Backer D. C., 1990, *ApJ*, **361**, 300
- Gaia Collaboration Prusti T., de Bruijne J. H. J., Brown A. G. A., Vallenari A., Babusiaux C., et al., 2016, *Astronomy and Astrophysics*, **595**, A1
- Gaia Collaboration Brown A. G. A., Vallenari A., Prusti T., de Bruijne J. H. J., Babusiaux C., Biermann M., 2020, eprints [arXiv:2012.01533](https://arxiv.org/abs/2012.01533)
- Gwinn C. R., Eubanks T. M., Pyne T., Birkinshaw M., Matsakis D. N., 1997, *Astrophysical Journal*, **485**, 87
- Hellings R. W., Downs G. S., 1983, *ApJ*, **265**, L39
- Hindmarsh M., Huber S. J., Rummukainen K., Weir D. J., 2017, *Phys. Rev. D*, **96**, 103520
- Hobbs D., et al., 2016, arXiv e-prints, p. [arXiv:1609.07325](https://arxiv.org/abs/1609.07325)

- Janssen G., et al., 2015, in *Advancing Astrophysics with the Square Kilometre Array (AASKA14)*, p. 37 ([arXiv:1501.00127](#))
- Jinno R., Takimoto M., 2017, *Phys. Rev. D*, **95**, 024009
- Kaiser N., Jaffe A., 1997, *ApJ*, **484**, 545
- Kelley L. Z., Blecha L., Hernquist L., Sesana A., Taylor S. R., 2017, *MNRAS*, **471**, 4508
- Klioni S. A., 2018, *Classical and Quantum Gravity*, **35**, 045005
- Lentati L., et al., 2015, *MNRAS*, **453**, 2576
- Li S.-L., Shao L., Wu P., Yu H., 2021, *arXiv e-prints*, p. [arXiv:2101.08012](#)
- Maggiore M., 2018, *Gravitational Waves. Vol. 2: Astrophysics and Cosmology*. Oxford University Press
- Middleton H., Sesana A., Chen S., Vecchio A., Del Pozzo W., Rosado P. A., 2021, *MNRAS*, **502**, L99
- Mignard F., Klioni S., 2012, *A&A*, **547**, A59
- Mihaylov D. P., Moore C. J., Gair J. R., Lasenby A., Gilmore G., 2018, *Phys. Rev. D*, **97**, 124058
- Mihaylov D. P., Moore C. J., Gair J. R., Lasenby A., Gilmore G., 2020, *Phys. Rev. D*, **101**, 024038
- Moore C. J., Mihaylov D. P., Lasenby A., Gilmore G., 2017, *Physical Review Letters*, **119**, 261102
- Nakai Y., Suzuki M., Takahashi F., Yamada M., 2021, *Physics Letters B*, **816**, 136238
- Neronov A., Pol A. R., Caprini C., Semikoz D., 2021, *Phys. Rev. D*, **103**, L041302
- O’Beirne L., Cornish N. J., 2018, *Phys. Rev. D*, **98**, 024020
- Paine J., Darling J., Graziani R., Courtois H. M., 2020, *ApJ*, **890**, 146
- Perera B. B. P., et al., 2019, *MNRAS*, **490**, 4666
- Planck Collaboration 2020, *A&A*, **641**, A6
- Pol N. S., et al., 2020, *arXiv e-prints*, p. [arXiv:2010.11950](#)
- Pyne T., Gwinn C. R., Birkinshaw M., Eubanks T. M., Matsakis D. N., 1996, *Astrophysical Journal*, **465**, 566
- Qin W., Boddy K. K., Kamionkowski M., Dai L., 2019, *Phys. Rev. D*, **99**, 063002
- Ratzinger W., Schwaller P., 2021, *SciPost Physics*, **10**, 047
- Sazhin M. V., 1978, *Soviet Ast.*, **22**, 36
- Schutz B. F., 2010, *Proceedings of the International Astronomical Union, IAU Symposium*, **261**, 234
- Schwaller P., 2015, *Phys. Rev. Lett.*, **115**, 181101
- Sesana A., 2013, *MNRAS*, **433**, L1
- Sesana A., Vecchio A., Colacino C. N., 2008, *MNRAS*, **390**, 192
- Shannon R. M., et al., 2015, *Science*, **349**, 1522
- Shapiro I. I., 1976, in *Methods in Experimental Physics*, Vol. 12, Astrophysics. Academic Press, pp 261–276
- Skilling J., 2004, in Fischer R., Preuss R., Toussaint U. V., eds, *AIP Conf. Proc.* Vol. 735, in proceedings. pp 395–405, [doi:10.1063/1.1835238](#)
- Smith T. L., Pierpaoli E., Kamionkowski M., 2006, *Phys. Rev. Lett.*, **97**, 021301
- Speagle J. S., 2020, *MNRAS*, **493**, 3132
- Theia Collaboration et al., 2017, *arXiv e-prints*, p. [arXiv:1707.01348](#)
- Titov O., Lambert S. B., Gontier A. M., 2011, *A&A*, **529**, A91
- Vagnozzi S., 2021, *Mon. Not. Roy. Astron. Soc.*, **502**, L11
- Vaskonen V., Veermäe H., 2021, *Phys. Rev. Lett.*, **126**, 051303
- Verbiest J. P. W., et al., 2016, *MNRAS*, **458**, 1267

## APPENDIX A: PTA MEASUREMENTS OF $\hat{\Omega}_{\text{GW}}(f)$

Measurements of the arrival time of pulses from an ensemble of millisecond pulsars provide a means to directly detect gravitational waves (GWs) in the nanohertz frequency window (Sazhin 1978; Detweiler 1979; Foster & Backer 1990). A PTA uses several large radio telescopes to make such measurements in every few weeks over a decade long period. A GW stochastic signal affects the time of arrival of the pulses from each of the pulsars in the array with a characteristic spatial correlation that depends on each pulsar pair’s angular separation in the sky described by the so-called Hellings and Downs correlation (Hellings & Downs 1983).

A planar GW from a source in direction  $\hat{q}$  causes a redshift in a pulsars pulse-frequency according to

$$z(t, \hat{q}) = \frac{1}{2} \frac{\hat{p}^i \hat{p}^j}{1 - \hat{q} \cdot \hat{p}} \Delta h_{ij}(t), \quad (\text{A1})$$

where  $\hat{p}$  is the direction to the pulsar, and  $\Delta h_{ij}(t)$  is the difference in spatial metric perturbations at the Earth (or solar system barycentre) at time  $t$  and the pulsar at retarded time  $t - D/c$ , where  $D$  is the distance to the pulsar. The actual measurable quantity in pulsar timing is the delay in pulse arrival time, or timing residual, given by

$$r(t) = \int^t dt' z(t'). \quad (\text{A2})$$

For an isotropic, stochastic signal, the timing residuals have a power-cross spectrum between pulsar  $a$  and  $b$  given by

$$S_{ab}(f) = \Gamma_{ab} \frac{A_{\text{CP}}^2}{12\pi^2} \left( \frac{f}{f_{\text{yr}}} \right)^{-\gamma} f_{\text{yr}}^{-3}. \quad (\text{A3})$$

Setting  $\Gamma_{ab} = 1$ , as there is currently no evidence for inter-pulsar correlations, gives  $S(f)$  as a function of frequency only, which can be related to  $h_c(f)$  or  $\hat{\Omega}_{\text{GW}}(f)$  used in the main text. Posteriors on the PT model spectra of all quantities are shown in Figs. 1 and D1.

Several constraints exist on the amplitude of a stochastic background exist from the 3 large independent PTA collaborations: Parkes PTA (PPTA; Shannon et al. 2015), the European PTA (EPTA; Lentati et al. 2015), NANOGrav (Arzoumanian et al. 2018). These PTAs, and others, collaborate under the umbrella of the international PTA (IPTA) which has also placed an upper limit on the GW background (IPTA; Verbiest et al. 2016).

Recently, NANOGrav (Arzoumanian et al. 2020) reported evidence for a stochastic common process (CP) among the 45 millisecond pulsars in their 12.5 year data set. Assuming this is due to an astrophysical GW foreground from supermassive BH binaries with the expected  $\gamma_{\text{CP}} = 13/3$  slope (Sesana et al. 2008; Sesana 2013; Kelley et al. 2017), the NANOGrav data are consistent with a GW signal with amplitude  $h_c(f_{\text{yr}}) = 1.37 - 2.67 \times 10^{-15}$  (5%–95%; using equation 1, this translates to the range on  $\hat{\Omega}_{\text{GW}}(f_{\text{yr}})$  stated in the main text) (Arzoumanian et al. 2020). Although, with no conclusive evidence for the inter-pulsar Hellings and Downs correlation, this cannot yet be regarded as a clear detection of GWs.

In our analysis, instead of the fiducial astrophysical model, we focus on the results of the NANOGrav free-spectrum analysis where the signal in each frequency bin is fitted separately. The most constraining measurements come at the lowest frequencies. As was done in Arzoumanian et al. (2020), we use the posteriors on the first 5 frequency bins. These measurements are plotted in Fig. 1 where it can be seen that the data are consistent with a wide range of GW spectral shapes which allows for a variety of non-standard interpretations, including the first-order dark-sector PTs considered here (Nakai et al. 2021; Ratzinger & Schwaller 2021; Addazi et al. 2020; Schwaller 2015), but also QCD PTs (Brandenburg et al. 2021; Neronov et al. 2021), topological defects (Ellis & Lewicki 2021; Blasi et al. 2021; Li et al. 2021; Abe et al. 2020), primordial BHs (De Luca et al. 2021; Vaskonen & Veermäe 2021) and inflation (Vagnozzi 2021).

## APPENDIX B: INTEGRATED CONSTRAINTS ON $\Omega_{\text{GW}}$

### B1 Cosmological

Cosmologically, a GW background behaves as a free-streaming gas of massless particles, in exactly in the same way as do neutrinos. It

therefore will have a similar effect on the growth of density perturbations in addition to its effect on the CMB via the expansion rate, including at the time of decoupling.

One then needs to consider the density distribution of the perturbations. This is related to the choice of an *adiabatic* or *homogeneous* spectrum of density perturbations. If the energy-density perturbations have the same density distribution as the other relativistic species they are said to be *adiabatic*. In this case the effects on the CMB, large-scale structure and baryon acoustic oscillations are indistinguishable from those of massless neutrinos. However, it is the cumulative effect of all relativistic species that is measured from CMB and large-scale structure observations. This is commonly parameterised in the literature as an effective number of relativistic species,  $N_{\text{eff}}$ .

Assuming adiabatic density perturbations, and using the third year WMAP data release (in combination with other small-scale CMB measurements, constraints from the Lyman- $\alpha$  forest and the Sloan Digital Sky Survey), [Smith et al. \(2006\)](#) obtain  $\Omega_{\text{GW}} h_{100}^2 \leq 4.0 \times 10^{-5}$  at 95% confidence ( $h_{100}$  is the present day Hubble constant in units of  $100 \text{ km s}^{-1} \text{ Mpc}^{-1}$ ). Using data from the Planck mission, [Clarke et al. \(2020\)](#) updated this bound and obtained  $\Omega_{\text{GW}} h_{100}^2 \leq 1.7 \times 10^{-6}$  (at 95% confidence). This integrated bound applies over a frequency range above  $f_{\text{min}} \sim 100 f_{\text{Hubble}} \sim 10^{-15} \text{ Hz}$ .

However, if the density perturbations are not adiabatic, this limit does not apply. If one instead assumes that the perturbations are initially homogeneous, then GW perturbations evolve differently to the neutrino perturbations and the degeneracy is broken. This modifies the growth of perturbations, especially at large scale. If the background is produced by some physical mechanisms that leaves its primordial density uncorrelated with the curvature perturbations – e.g. phase transitions, and anything post-inflation – then this alternate limit applies ([Smith et al. 2006](#)). Using the WMAP data they obtain  $\Omega_{\text{GW}} h_{100}^2 \leq 8.4 \times 10^{-6}$  at 95% confidence, which is *tighter* than under the adiabatic assumption. This bound has been revised using recent Planck data to yield  $\Omega_{\text{GW}} h_{100}^2 \leq 2.9 \times 10^{-7}$  by [Clarke et al. \(2020\)](#). This alternate bound also applies over a frequency range above  $f_{\text{min}} \sim 100 f_{\text{Hubble}} \sim 10^{-15} \text{ Hz}$ .

Big bang nucleosynthesis (BBN) bounds on  $\Omega_{\text{GW}}$  come from the measured primordial abundance of light atomic nuclei. The theoretical prediction of the abundances of these elements (including D,  $^3\text{He}$ ,  $^4\text{He}$ , and  $^7\text{Li}$ ) is among the most impressive achievements of modern concordance cosmology. The bounds on  $\Omega_{\text{GW}}$  come from the dependence of the abundances on the expansion rate of the universe at the time of BBN which occurs at a temperature  $T_{\text{BBN}} \sim 1 \text{ MeV}$ . [Cooke et al. \(2014\)](#) and [Maggiore \(2018\)](#) find a bound of  $\Omega_{\text{GW}} h_{100}^2 \leq 1.3 \times 10^{-6}$ . Although this bound is also coupled with the effective number of neutrinos. The minimum frequency over which the integrated BBN bound applies is set by the horizon scale at the time of BBN, redshifted to the present day. Taking  $T_{\text{BBN}} \sim 1 \text{ MeV}$ , this gives  $f_{\text{min}} = f_{\text{BBN}} \sim 10^{-10} \text{ Hz}$ , although, in reality, there is a smooth transition over a range of frequencies  $\sim 10^{-12} - 10^{-10} \text{ Hz}$ . For the PT models considered here, the frequency range over which the BBN bound is obtained is less constraining than that for the CMB bound. This is because the PT models can have a large fraction of their total energy at frequencies  $f < f_{\text{BBN}}$ , thereby partially evading the BBN constraint (see arrows in Fig. 1).

For both the the CMB and BBN bounds, the upper limit of frequency sensitivity is effectively  $f_{\text{max}} \rightarrow \infty$  as the only known limit on the GW wavelength is set by Planck-scale physics at the relevant cosmological time.

## B2 Astrometric

The idea that GWs cause observable astrometric effects in optical sources is an old one ([Braginsky et al. 1990](#); [Kaiser & Jaffe 1997](#)) but the prospects for a detection are generally not considered promising ([Schutz 2010](#)). For a distant optical source, such as a quasar (QSO), in direction  $n^i$ , the GW induced astrometric deflection  $\delta n^i$  depends on the local GW metric perturbation in the solar system,  $h_{ij}$ , caused by a GW source in direction  $q^i$ . The deflection is given by [[Pyne et al. \(1996\)](#), see also [Book & Flanagan \(2011\)](#); [Mihaylov et al. \(2018\)](#)]

$$\delta n^i(t) = \left[ \frac{(n^i - q^i)n^j n^k}{2(1 - q_l n^l)} - \frac{1}{2} \delta^{ij} n^k \right] h_{jk}(t). \quad (\text{B1})$$

Early efforts to detect this effect used very long baseline interferometry (VLBI) ([Shapiro 1976](#)) measurements of the positions of radio sources. However, interest increased following the launch of Gaia ([Gaia Collaboration et al. 2016](#)) and the early data releases.

Focusing, for the moment, on the Gaia eDR3 release ([Gaia Collaboration et al. 2020](#)) (which has a duration of 34 months  $\approx 10^8 \text{ s}$ ), there are two distinct frequency regimes in GWs can potentially be detected. In the range  $f \gtrsim 10^{-8} \text{ Hz}$ , Gaia can look for periodic effects of GWs with periods shorter than the mission duration; see, for example, [Moore et al. \(2017\)](#); [Klioner \(2018\)](#). Alternatively, for ultra-low GW frequencies, Gaia can search for the secular effects of GWs with periods longer than the mission duration; see, for example [Mignard & Klioner \(2012\)](#). It is the later case that is our focus here. Unlike PTA observations which directly constrain the GW spectrum  $\hat{\Omega}_{\text{GW}}(f)$ , astrometric observations taken over time span  $T$  place constraints on the integrated spectrum  $\Omega_{\text{GW}}$  with  $f_{\text{max}} \sim 1/T$ . The lower frequency sensitivity is only limited by the Hubble scale,  $f_{\text{min}} \sim f_{\text{Hubble}}$ .

As in pulsar timing, the *smoking gun* signature of stochastic GW background would be a distinctive correlation in the pattern of QSO proper motions. This correlation pattern is predominantly quadrupolar (i.e.  $\ell = 2$ ) but with subdominant contributions from higher harmonics ([Book & Flanagan 2011](#)) [see also [Mihaylov et al. \(2018\)](#), and [Qin et al. \(2019\)](#) for a discussion using an alternative formalism] and can be thought of as the astrometric analog of the PTA Hellings and Downs curve. This correlation pattern is an extremely robust predict within the theory of general relativity as it depends on no free parameters. Measuring this correlation pattern can be a powerful test of the theory as it is sensitive to both the polarisation context of the GW background and the propagation speed of the GWs ([Mihaylov et al. 2018](#); [O’Beirne & Cornish 2018](#); [Mihaylov et al. 2020](#)). (See also [Qin et al. \(2019\)](#) for an alternative approach.)

Early astrometric constraints on the GW background came from VLBI. [Gwinn et al. \(1997\)](#) used measurements of 323 extragalactic sources to place the constraint  $\Omega_{\text{GW}} \lesssim 10^{-1}$  with  $f_{\text{max}}^{-1} \sim 10 \text{ year}$ . This was subsequently improved by [Titov et al. \(2011\)](#) to  $\Omega_{\text{GW}} \lesssim 4 \times 10^{-3}$  with  $f_{\text{max}}^{-1} \sim 20 \text{ year}$  using 555 sources. Both analyses used only the quadrupolar component of the proper motions.

Prior to launch, several studies attempted to forecast the improvement on this bound that might be expected by the end of the Gaia mission. Gaia will observe a much larger catalog of several million QSOs, albeit with larger proper motion errors than obtained with VLBI. [Book & Flanagan \(2011\)](#) projected a constraint of  $\Omega_{\text{GW}} \lesssim 10^{-6}$  with  $f_{\text{max}}^{-1} \sim 1 \text{ year}$ . A more conservative assessment by [Mignard & Klioner \(2012\)](#) projected  $\Omega_{\text{GW}} \lesssim 8 \times 10^{-5}$  with  $f_{\text{max}}^{-1} \sim 5 \text{ year}$ .

More recently, [Darling et al. \(2018\)](#) placed an updated VLBI constraint of  $\Omega_{\text{GW}} \lesssim 6 \times 10^{-3}$  with  $f_{\text{max}}^{-1} \sim 20 \text{ year}$  using 713 radio sources and  $\Omega_{\text{GW}} \lesssim 10^{-2}$  with  $f_{\text{max}}^{-1} \sim 1 \text{ year}$  using Gaia DR1 in combination with a smaller set of 508 VLBI sources. [Darling et al.](#)

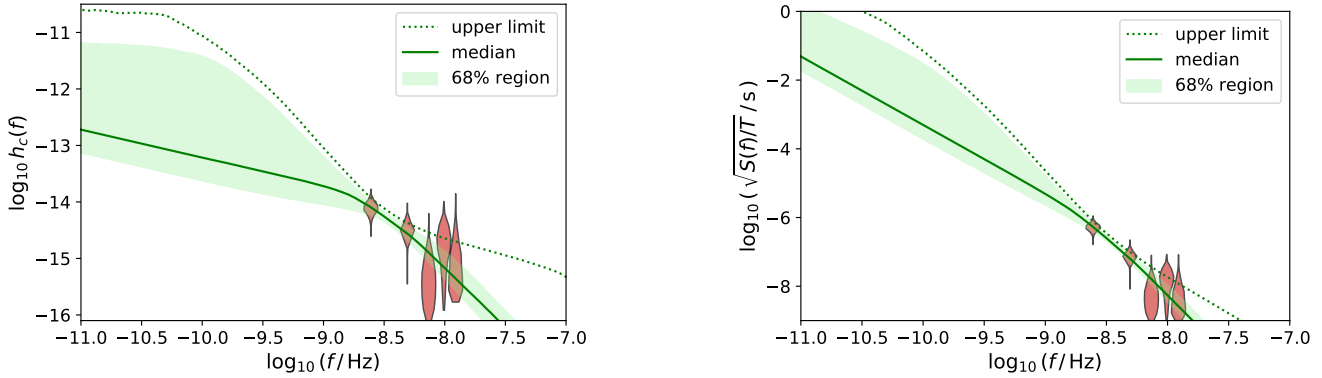


**Figure D1.** Transformed posteriors on the PT spectrum shown in Fig. 1 that were obtained from the 5 lowest frequency bins of the NANOGrav free-spectrum model (red). Left: the characteristic strain,  $h_c(f)$ , defined in equation 1. Right: the delay, defined as  $\sqrt{S(f)}/T$ , where the power cross spectrum  $S(f)$  is defined in equation A3 and  $T = 12.5$  years is the duration of the observations.

(2018) also used primarily the quadrupole component of the proper motions in their analysis, but also considered octupole contributions.

Further improvements might be expected due to: (i) longer baselines out to  $\approx 10$  years in future Gaia data releases, (ii) larger data sets with more QSOs and better source selection, (iii) reduced astrometric errors and improved control over systematics, (iv) consistent inclusion of higher harmonics in the analysis, (v) simultaneous inclusion of different astrometric datasets obtained over different baselines and that therefore constrain the integrated spectrum over different frequency bandwidths (extra care will be required if datasets are not independent, as would be the case with different Gaia data releases). However, see also Paine et al. (2020) who point out some of difficulties that need to overcome to maximise the astrometric GW sensitivity. Longer term, future astrometric observatories (Hobbs et al. 2016; Theia Collaboration et al. 2017) might also place tighter constraints.

### APPENDIX C: ANALYSIS

We use the NANOGrav  $T = 12.5$  year posteriors (Arzoumanian et al. 2020) on the delay,  $\sqrt{S(f_i)}/T$ , at the 5 lowest frequencies,  $f_i$ . These posteriors are from the free spectrum analysis in which the amplitude of the GW spectrum in each frequency bin is allowed to vary independently. We use the public data products from <https://data.nanograv.org>. These posteriors were converted to  $\hat{\Omega}_{\text{GW}}(f_i)$  via equations 1 and A3 and used to build kernel density estimates (KDEs) for the posterior at each frequency.

We consider two models for the spectrum,  $\hat{\Omega}_{\text{GW}}(f)$ . First, the physically motivated PT model from Caprini et al. (2009); Jinno & Takimoto (2017); Hindmarsh et al. (2017), for which we use the semi-analytic parameterisation described in Arzoumanian et al. (2021). This contains 4 free parameters: the temperature,  $T_*$ , and strength,  $\alpha_*$ , of the transition, the dimensionless nucleation rate  $\beta/H_*$ , and the dimensionless friction parameter,  $\eta$ . For each of these parameters we use log-uniform priors over the ranges shown in Fig. 3. Second, the simple power-law model which is described by just an amplitude,  $A_{\text{CP}}$ , and spectral slope,  $\gamma_{\text{CP}}$ . Uniform (log-uniform) priors on  $\gamma_{\text{CP}}$  ( $A_{\text{CP}}$ ) over the ranges shown in Fig 2 were used. The power-law model also requires low and high frequency cutoffs; these were fixed during inference runs and results are shown for several choices.

Our PTA-only log-likelihood function is obtained by evaluating the spectrum at the 5  $f_i$  and summing the log-PDFs of the 5 independent KDEs at these values. If required, an integrated constraint is imposed

by setting the log-likelihood to  $-\infty$  if the integrated energy across all frequencies exceeds  $\Omega_{\text{GW}} > 10^{-6}$ . Sampling was performed with the DYNESTY (Speagle 2020) implementation of the nested sampling algorithm (Skilling 2004). Posteriors on the PT parameters are shown in Fig. 2 and for the power-law parameters in Fig. 3.

It should be pointed out that our PTA-only analysis differs from that in Arzoumanian et al. (2021) where the 12.5 year data set was reanalysed in its entirety, which includes marginalising again over the red-noise parameters in each pulsar. Here we exploit the posterior density functions on the 5 lowest frequency bins that have already been obtained from a previous full free spectrum analysis that has already marginalised over the red-noise parameters. We use these posterior samples to perform a second Bayesian analysis on the GW background parameters only. In this sense, ours is a hierarchical analysis. The agreement between the two approaches can be clearly seen by comparing Fig. 3 with Fig. 4 in Arzoumanian et al. (2021). This hierarchical approach allows for an easy modification of the likelihood to include additional information, such as the integrated constraints considered here. Our approach can therefore be used in future to analyse multiple datasets and explore a wider range of possible GW production mechanisms.

### APPENDIX D: ADDITIONAL PLOTS

Fig. D1 shows the same results as Fig. 1 in the main text transformed into other commonly used quantities in the literature.

This paper has been typeset from a  $\text{\TeX}/\text{\LaTeX}$  file prepared by the author.